Inhibitors of histone acetyltransferases KAT6A/B induce senescence and arrest tumor growth

Jonathan B. Baell[1,2*], David J. Leaver[1], Stefan J. Hermans[3], Gemma L. Kelly[4,5], Margs S. Brennan[4,5], Natalie L. Downer[4], Nghi Nguyen[1], Johannes Wichmann[4,5], Helen M. McRae[4,5], Yuqing Yang[4,5], Ben Cleary[1], H. Rachel Lagiakos[1,6], Stephen Mieruszynski[4,5], Guido Pacini[4,5], Hannah K. Vanyai[4,5], Maria I. Bergamasco[4,5], Rose E. May[4], Bethany K. Davey[6], Kimberly J. Morgan[4,5], Andrew J. Sealey[4,5], Beinan Wang[4,5,7], Natasha Zamudio[4,5], Stephen Wilcox[4,5], Alexandra L. Garnham[4], Bilal N. Sheikh[4,5], Brandon J. Aubrey[4,5], Karen Doggett[4,5], Matthew C. Chung[3], Melanie de Silva[4,6], John Bentley[8], Pat Pilling[8], Meghan Hattarki[8], Olan Dolezal[8], Matthew Dennis[8], Hendrik Falk[4,5,6], Bin Ren[8], Susan A. Charman[9], Karen L. White[9], Jai Rautela[4,5], Andrea Newbold[11], Edwin D. Hawkins[4,5], Ricky W. Johnstone[11], Nicholas D. Huntington[4,5], Thomas S. Peat[8], Joan K Heath[4,5], Andreas Strasser[4,5], Michael W. Parker[3,10], Gordon K. Smyth[4,12], Ian P. Street[4,5,6], Brendon J. Monahan[4,5,6], Anne K. Voss[4,5,#*] and Tim Thomas[4,5,#*]

[1] *Medicinal Chemistry Theme, Monash Institute of Pharmaceutical Sciences, Monash University, Parkville, Victoria, Australia*
[2] *School of Pharmaceutical Sciences, Nanjing Tech University, No. 30 South Puzhu Road, Nanjing 211816, People's Republic of China*
[3] *ACRF Rational Drug Discovery Centre, St. Vincent's Institute of Medical Research, Fitzroy, Victoria, Australia*
[4] *The Walter and Eliza Hall Institute of Medical Research, Parkville, Victoria, Australia.*
[5] *Department of Medical Biology, University of Melbourne, Parkville, Victoria, Australia.*
[6] *Cancer Therapeutics CRC, 343 Royal Parade, Parkville, Victoria, Australia.*
[7] *School of Pharmaceutical Science, Tsinghua University, Haidian, Beijing, China*
[8] *Commonwealth Scientific and Industrial Research Organisation (CSIRO), Biomedical Program, Parkville, Victoria, Australia.*
[9] *Centre for Drug Candidate Optimisation, Monash Institute of Pharmaceutical Sciences, Monash University, Parkville, Victoria, Australia*
[10] *Department of Biochemistry and Molecular Biology, Bio21 Molecular Science and Biotechnology Institute, University of Melbourne, Parkville, Victoria, Australia*
[11] *The Peter MacCallum Cancer Centre, Melbourne, Victoria 3000, Australia*
[12] *Department of Mathematics and Statistics, University of Melbourne, Parkville, Victoria, Australia*
 # These authors share senior authorship

Keywords: KAT6A; MYST3; MOZ; senescence; lysine acetyltransferase; small molecule inhibitors.

*Corresponding authors:

Tim Thomas, 1G Royal Parade, Melbourne 3052, Victoria, Australia, e-mail: tthomas@wehi.edu.au Ph: +61 3 9345 2477 Fax: +61 3 9347 0852

Jonathan Baell, 381 Royal Parade, Parkville, Victoria 3052, Australia, e-mail: Jonathan.Baell@monash.edu Ph: +61 3 9903 9044 Fax: +61 3 9903 9581

Anne K. Voss, 1G Royal Parade, Melbourne 3052, Victoria, Australia, e-mail: avoss@wehi.edu.au Ph: +61 3 9345 2477 Fax: +61 3 9347 0852

Acetylation of histones by lysine acetyltransferases (KATs) is essential for chromatin organization and function.[1] The MYST family of KATs (KAT5-8) includes the oncogenes *KAT6A* (*MOZ*) and *KAT6B* (*MORF/QKF*).[2,3] KAT6A has essential roles in normal hematopoietic stem cells[4-6] and is the target of recurrent chromosomal translocations, causing acute myeloid leukemia.[7,8] Similarly, chromosomal translocations in *KAT6B* have been identified in diverse cancers.[8] KAT6A suppresses cellular senescence via regulation of suppressors of the *CDKN2A* locus,[9,10] a function that requires its KAT activity.[10] Loss of one allele of *KAT6A* extends the median survival of mice with MYC-induced lymphoma from 105 to 413 days.[11] These findings suggest that inhibition of KAT6A and KAT6B may provide a therapeutic benefit in cancer. We have produced a series of highly potent, selective inhibitors of KAT6A/B including WM-8014 and WM-1119. Biochemical and structural studies demonstrate that these compounds are reversible acetyl-CoA competitors and inhibit MYST-catalyzed histone acetylation. WM-8014 and WM-1119 induce cell cycle exit and cellular senescence without causing DNA damage. Senescence is INK4A/ARF dependent and accompanied by gene expression changes typical of loss of KAT6A function. WM-8014 potentiates oncogene-induced senescence in vitro and in a zebrafish model of hepatocellular carcinoma. WM-1119, with improved bioavailability, arrests lymphoma progression in mice. We anticipate that this class of inhibitors will be useful in accelerating development of therapeutics targeting gene transcription regulated by histone acetylation.

We screened 243,000 diverse small molecule compounds[12] to discover the sulfonylhydrazide compound CTx-0124143, a competitive KAT6A inhibitor (IC_{50} 0.49 μM) in biochemical assays.[12] Medicinal chemistry optimization yielded WM-8014 with an IC_{50} of 8 nM (Fig. 1a, Supplementary Table 1), thus increasing the KAT6A inhibitory activity by 60-fold; this was consistent with the kinetic affinity value (K_D) of 5 nM derived from surface plasmon resonance (SPR) measurements (Fig. 1a, Extended Data Fig. 1). WM-8014 inhibits predominantly the closely related KAT6A and KAT6B (respective IC_{50}: 8 nM, 28 nM) and is more than 10-fold less active against KAT7 and KAT5 (respective IC_{50}: 342 nM, 224 nM; Fig. 1b; Supplementary Table 1). SPR kinetic binding curves demonstrated that the interaction of this compound class with immobilized proteins was fully reversible and

consistent with a single-site binding interaction. The interaction of WM-8014 with KAT6A and KAT7, although relatively strong, was in both cases driven by fast association kinetics (k_a > 1 x 10^6 $M^{-1}s^{-1}$) whilst the dissociation kinetics (k_d ~ 4 x 10^{-2} for KAT6A and 17 x 10^{-2} s^{-1} for KAT7) were indicative of a relatively short-lived lifespan of the binary complex (Extended Data Fig. 1). WM-8014 displayed an order of magnitude weaker binding to KAT7 (K_D: 5.1 vs. 52 nM) (Fig. 1b; Extended Data Fig. 1). We also generated an inactive analogue WM-2474 (Fig. 1a, Supplementary Table 1). Surprisingly, these compounds were almost inactive against KAT8 and no inhibition was observed for the more distantly related lysine acetyltransferases KAT2A/B and KAT3A/B (Fig. 1 b,c; Supplementary Table 1).

The physicochemical properties of WM-8014 show desirable drug-like properties (Supplementary Table 2), being completely stable in cell culture media; however relatively high protein binding (97.5%) in this media (10% fetal calf serum) reduces the free concentration. Although WM-8014 showed relatively low solubility in water (8-16 μM), due to its high lipophilicity (cLogP 4.1; cLogD 3.8 at physiological pH), Caco-2 cells were highly permeable to WM-8014 (Papp 78 ± 13 x 10^{-6} cm/s). Testing of WM-8014 at 1 μM and 10 μM against a pharmacological panel of 158 diverse biological targets revealed no significant affinity, with only 8 enzymes showing greater than 50% binding (Supplementary Table 3).

The crystal structures of a modified MYST histone acetyltransferase domain ($MYST^{Cryst}$,) in complex with WM-8014 (1.85 Å resolution, Fig. 1 d-f, Extended Data Fig. 1, Supplementary Table 4) or acetyl coenzyme A (AcCoA; 1.95 Å resolution, (Fig. 1g) were solved. The WM-8014 molecule occupies the AcCoA binding site on $MYST^{Cryst}$, being partially enclosed between α-helix D685-R704 and the loop extending from Q654-G657. The $MYST^{Cryst}$:AcCoA complex adopts a globular fold (Fig. 1g), as previously reported structures,[13] with an (rmsd: 0.6 Å) and is nearly identical to the $MYST^{Cryst}$:WM-8014

complex (rmsd of 0.3 Å for all aligned atoms). Accordingly, the core sulfonylhydrazide moiety of WM-8014 makes similar hydrogen bonds to $MYST^{Cryst}$ as the diphosphate group of AcCoA (Fig. 1f,g). This includes hydrogen bonds to the main-chain atoms of R655, G657, and R660 identical to AcCoA, as well as additional hydrogen bonds to G659 and S690 (Extended Data Fig. 1). The biphenyl group of WM-8014 extends further into the AcCoA binding pocket, allowing van der Waals interactions with residues L601, I647, I649, S684, and L686 of $MYST^{Cryst}$ (Extended Data Fig. 1). Thus, WM-8014 competes directly with AcCoA in the substrate-binding domain.

Since KAT6A suppresses senescence[12,13] we examined the ability of WM-8014 to induce cell cycle arrest in E13.5 mouse embryonic fibroblasts (MEFs). WM-8014-treated cells failed to proliferate after 10 days of treatment (Fig. 2a; IC_{50} of 2.4 μM), with similar kinetics to Cre-recombinase *Kat6a* recombination (Fig. 2b). Higher doses of WM-8014 (up to 40 μM) did not significantly accelerate growth arrest, which after 8 days of treatment was irreversible, (Extended Data Fig. 2). The inactive compound WM-2474 did not affect cell proliferation. Cell cycle analysis showed an increase in the proportion of cells in G_0-G_1 after 4 days of treatment and a corresponding reduction in cells in G_2-M and S phases, both in Fucci cells[14] and in BrdU incorporation assays (Fig. 2c, Extended Data Fig. 2).

RNA sequencing showed MEFs treated with WM-8014 upregulate *Cdkn2a* mRNA expression (day 10: FDR < 10^{-6}; Fig. 2d) and decreased expression of *Cdc6* (day 10: FDR < 10^{-6}; Fig. 2d), a KAT6A target gene[9] and repressor of the *Cdkn2a* locus[15] and showed substantial increase in ß-galactosidase activity (Fig. 2e), which are markers of senescent cells, accompanied by typical morphological changes (Extended Data Fig. 2). WM-8014 caused a concentration-dependent reduction in the level of *E2f2* mRNA (adj. $R^2 = 0.73$; $p < 0.0005$) and *Cdc6* mRNA (adj. $R^2 = 0.5$; $p = 0.002$) accompanied by up-regulation of both splice

products of the *Cdkn2a* locus, *Ink4a* and *Arf* (day 10: $p < 0.0005$ and $p = 0.005$, respectively; Extended Data Fig. 3). Importantly, MEFs treated for 4 days or 10 days with 10 μM WM-8014, the control compound WM-2474 or vehicle DMSO showed no change in the levels of γH2A.X (Extended Data Fig. 4), suggesting cell cycle arrest was not a consequence of DNA damage. No increase in apoptosis or necrosis was seen (Extended Data Fig. 4). Treatment of either *Trp53* or *Cdkn2a* null (*Ink4a*$^{-/-}$;*Arf*$^{-/-}$) MEFs with WM-8014 had a minor or no effect on cell proliferation, respectively (Fig. 2f). These results show that WM-8014 acts via the $p16^{INK4A}$-$p19^{ARF}$ pathway, to cause irreversible cell cycle exit leading to senescence and does not have a general cytotoxic effect.

KAT7 is essential for global histone 3 lysine 14 (H3K14) acetylation.[16]. In contrast, KAT6A regulates H3K9 acetylation only at target loci.[17,18]**.** We determined the effects of WM-8014 on global levels of acetylation at H3K9 and H3K14 by western blot after 5 days of treatment. Treatment with 10 μM WM-8014 caused a 49% decrease in global levels of H3K14ac, but as expected based on KAT6A's locus-specific roles,[17,18] not global H3K9ac (Fig. 3a,b; all gel source data in Supplementary Figure 1). The effects of WM-8014 on global H3K14ac levels were concentration-dependent (Fig. 3b; H3K14ac/H4 ratio regressed on log concentration of WM-8014; adj. $R^2 = 0.76$, $p < 0.001$; $IC_{50} = 1.2$ μM). RNA-sequencing showed a strong correlation between the gene expression changes seen in *Kat6a*$^{-/-}$ vs. *Kat6a*$^{+/+}$ MEFs and genes differentially expressed after WM-8014 treatment (WM-8014 vs. inactive WM-2474), with a 2.6-fold enrichment in upregulated genes (FDR 0.0001; Fig. 3c) and a 2.1-fold enrichment in downregulated genes (FDR 0.0001; Fig. 3c) and gene expression signatures characteristic of cellular senescence (Extended Data Fig. 5). Loss of KAT6A results in the downregulation of *E2f2*, *Ezh2*, and *Melk*.[9] Similarly, treatment with WM-8014 caused significant downregulation of *Ezh2*, *Melk* and *E2f2* mRNA levels compared with controls (Fig. 3d); determined by RNA-seq (Extended Data Fig. 5) and confirmed by RT-qPCR

153 (Extended Data Fig. 3). After treatment with WM-8014 there was a reduction of H3K9ac at
154 the transcription start sites (TSS) of these genes (Fig. 3e). Thus, treatment of cells with WM-
155 8014 directly inhibits global H3K14 acetylation catalyzed by KAT7, when used at high
156 concentrations, and KAT6A-specific H3K9 acetylation at transcription start sites.
157
158 Since WM-8014 induced cellular senescence, we reasoned that it might exacerbate oncogenic
159 RAS-induced senescence. Accordingly, MEFs expressing a constitutively active form of
160 RAS, ($HRAS^{G12V}$), were more sensitive to WM-8014 inducing cell cycle arrest (Extended
161 Data Fig. 6). We then examined the effects of WM-8014 in a zebrafish model[19] of
162 $KRAS^{G12V}$-driven hepatocellular over proliferation. We observed a significant, concentration-
163 dependent reduction in liver volume in response to treatment with WM-8014 and a
164 substantial reduction in hepatocytes in S-phase (Extended Data Fig. 6). Surprisingly, WM-
165 8014 did not impair the growth of the normal liver, demonstrating that the inhibitory effects
166 of WM-8014 were specific to hepatocytes expressing oncogenic RAS. Oncogenic $KRAS^{G12V}$
167 expressing, but not control hepatocytes treated with WM-8014 robustly upregulated the cell
168 cycle regulators *Cdkn2a* and *Cdkn1a*. Thus, WM-8014 potentiates oncogene-induced
169 senescence, but does not affect normal hepatocyte growth.
170
171 Lymphoma progression is highly dependent on KAT6A, since *Kat6a* heterozygous mice are
172 protected from early onset MYC driven lymphoma.[11] However, the high plasma protein
173 binding characteristics of WM-8014 (Supplementary Table 2) precluded in vivo studies in
174 mice. Therefore, we developed further compounds resulting in WM-1119, which has reduced
175 plasma protein binding (Fig. 4a; Supplementary Table 2). The interaction of WM-1119 with
176 KAT6A is similar to WM-8014: characterized by strong reversible binding (WM-1119: IC_{50}
177 2 vs. 8 nM in WM-8014; Extended Data Fig. 7) competitive with AcCoA and driven by fast
178 association kinetics ($k_a > 1 \times 10^6$ $M^{-1}s^{-1}$; Extended Data Fig. 7). The structures of $MYST^{Cryst}$

179 in complex with WM-1119 was solved (Extended Data Fig. 7, Supplementary Table 5) and
180 was almost identical to that of $MYST^{Cryst}$:WM-8014, with an rmsd for aligned main-chain
181 atoms of 0.2 Å. The key differences are an additional hydrogen bond between the WM-1119
182 pyridine nitrogen and main-chain of I649 (Extended Data Fig. 7) and the hydrophobic
183 interaction between the meta-methyl of the biphenyl group of WM-8014 and I663 is lost in
184 WM-1119. Interestingly, WM-1119 is 1100-fold and 250-fold more active against KAT6A
185 than KAT5 or KAT7, respectively (Fig. 4a, Extended Data Fig. 7), and so more specific for
186 KAT6. Testing of WM-1119 at 1 μM and 10 μM against a pharmacological panel of 159
187 diverse biological targets revealed no significant affinity (Supplementary Table 6). WM-1119
188 treatment of MEFs resulted in cell cycle arrest in G_1 and a senescence phenotype similar to
189 WM-8014 (Extended Data Fig. 8). Notably, WM-1119 has 19-fold greater activity in this
190 cell-based assay than WM8014 (IC_{50}: ~ 0.126 μM vs. 2.4 μM) and is able to induce cell cycle
191 arrest at 1 μM.
192
193 To test inhibitors of KAT6A in a cancer model we investigated the effect of WM-1119 and
194 WM-8014 on lymphoma cell proliferation. The B cell lymphoma cell line, EMRK1184,
195 which was isolated from mice with a tumor resulting from the expression of *cMyc* under the
196 control of the IgH enhancer[20] was selected, because it expressed the *Cdnk2a* locus-encoded
197 ARF and wild type p53 (Extended Data Fig. 9). Treatment with WM-8014 or WM-1119
198 inhibited the proliferation of the EMRK1184 lymphoma cells in vitro (Fig. 4b), RNA-seq and
199 Western blot analysis showed that WM-1119 treatment resulted in increased levels of
200 *Cdkn2a* and *Cdkn2b* mRNA and $P16^{INK4a}$ and $p19^{ARF}$ protein, as well as a delayed increase in
201 *Cdkn1a* mRNA (Extended Data Fig. 9). WM-1119 (IC_{50}: 0.25 μM) was 9-fold more active
202 than WM-8014 (IC_{50}: 2.3 μM; Fig. 4b), as expected based on reduced protein binding
203 (Supplementary Table 2).

We tested the effectiveness of KAT6 inhibitors in the treatment of lymphoma within the whole mouse. C57BL/6-albino (B6(Cg)-Tyr^{c-2J}/J) mice were injected intravenously with 100,000 EMRK1184 cells transfected with a luciferase-expression construct. Lymphoma growth was monitored using the IVIS imaging system. Three days after lymphoma cell transplant, all mice showed luciferase activity (Fig. 4c) indicating the expansion of lymphoma cells. Mice were then divided randomly into WM-1119 treatment and vehicle control groups. Since WM-1119 is rapidly cleared after intraperitoneal injection with the plasma concentration dropping below 1 μM after 4-6 h (Extended Data Fig. 9), cohorts of mice were injected every 8 h (3x/day, 2 cohorts of 3 mice/treatment group) or every 6 h (4x/day, 2 cohorts of 3 and 6 mice/treatment group) (Fig. 4d). Mice were imaged 5x over the course of these experiments to monitor the growth of lymphoma. No significant difference between treatment and control groups was seen before Day 10 (Fig. 4d, Extended Data Fig. 10), which was expected since inhibition of cell proliferation *in vitro* took ~7 days. However, by day 14 the 4x/day WM-1119 treated cohorts had cleared almost all tumor cells (Fig 4c, Extended Data Fig. 10), with the exception of 1 mouse that did not respond (Fig. 4d). Spleen weights in the WM-1119 treatment group (4x/day) were substantially lower than spleen weights in the vehicle treated group and not significantly different from tumor-free 8-week old mice ($p < 0.0005$ and $p = 1$, respectively; Fig. 4e,f). Treatment with WM-1119 3x/day led to a significant reduction in tumor burden and spleen weight, but was not as effective as 4x/day treatment (Fig. 4d,f). WM-1119 was well tolerated; mice showed no generalized ill effects and did not suffer weight loss (Extended Data Fig. 10). WM-1119 treatment had no effect on hematocrit, erythrocytes or platelet numbers, but there was an overall leukopenia (Extended Data Fig. 10). The proportion and overall number of tumor cells was substantially reduced by WM-1119 treatment (4x/day; Fig. 4g). Intracellular flow cytometric analysis demonstrated a reduction in H3K9ac in tumor cells ($p = 0.03$; Extended Data Fig. 10). These results demonstrate that WM-1119 is effective in treating lymphoma *in vivo*.

In summary, using high throughput screening followed by medicinal chemistry optimization, in-cell assays, biochemical assessment of target engagement and tumor models in mice and fish, we have developed a novel class of inhibitors for a hitherto unexplored category of epigenetic regulators. These inhibitors engage the MYST family of lysine acetyltransferases in primary cells and specifically induce cell cycle exit and senescence and are effective in preventing lymphoma progression in mice.

Acknowledgments

We thank Faye Dabrowski, Cassandra D'Alessandro, WEHI Bioservices, the WEHI FACS laboratory, the MX2 beamline staff at the Australian Synchrotron for their expert help and Zhiyuan Gong for the two transgenic zebrafish lines. This work was funded by the Australian Government through NHMRC Project Grants 1030704, 1080146, Research Fellowships (TT, AKV, GKS, JKH, MWP, JB), the NHMRC IRIISS and the Cancer Therapeutics Cooperative Research Centre. The Victorian State Government OIS Grants to WEHI, Monash and St Vincent's Institute are gratefully acknowledged.

Author Information

The authors declare no financial or non-financial competing interest. Requests for reprints, permissions, and materials can be addressed to the corresponding authors.

Author contribution

TT was responsible for initiating the project. TT and AKV supervised the project, performed experiments and wrote the manuscript. Medicinal chemistry: JBB, DJL, NN, BC, HRL. Structural biology, SJH, MCC, BR, TSP, MWP. Chemical screening, protein biochemistry

and assays: MdS, JB, PP, MH, OD, MD, HF, IPS, BJM. Pharmacology: SAC, KLW. Bioinformatics: GP, ALG, GKS. Cell based assays, molecular biology and biochemistry: NLD, JW, HMM, YY, HKV, MIB, REM, BKD, BW, NZ, SW, BNS, BJA. Zebrafish model: SM, KJM, AJS, KD, JKH . Mouse cancer models GLK, MSB, JR, AN, EDH, RWJ, NDH, AS.

References

1 Lee, K. K. & Workman, J. L. Histone acetyltransferase complexes: one size doesn't fit all. *Nat Rev Mol Cell Biol* **8**, 284-295 (2007).

2 Allis, C. D. *et al.* New nomenculature for chromatin-modifying enzymes. *Cell* **633-36**, 1-4 (2007).

3 Voss, A. K. & Thomas, T. MYST family histone acetyltransferases take center stage in stem cells and development. *Bioessays* **31**, 1050-1061 (2009).

4 Katsumoto, T. *et al.* MOZ is essential for maintenance of hematopoietic stem cells. *Genes Dev* **20**, 1321-1330 (2006).

5 Thomas, T. *et al.* Monocytic leukemia zinc finger protein is essential for the development of long-term reconstituting hematopoietic stem cells. *Genes Dev* **20**, 1175-1186 (2006).

6 Sheikh, B. N. *et al.* MOZ (KAT6A) is essential for the maintenance of classically defined adult hematopoietic stem cells. *Blood* **128**, 2307-2318 (2016).

7 Borrow, J. *et al.* The translocation t(8;16)(p11;p13) of acute myeloid leukaemia fuses a putative acetyltransferase to the CREB-binding protein. *Nat Genet* **14**, 33-41 (1996).

8 Huang, F., Abmayr, S. M. & Workman, J. L. Regulation of KAT6 Acetyltransferases and Their Roles in Cell Cycle Progression, Stem Cell Maintenance, and Human Disease. *Mol Cell Biol* **36**, 1900-1907 (2016).

9 Sheikh, B. N. *et al.* MOZ (MYST3, KAT6A) inhibits senescence via the INK4A-ARF pathway. *Oncogene* **34**, 5807-5820 (2015).

10 Perez-Campo, F. M. *et al.* MOZ-mediated repression of p16(INK4a) is critical for the self-renewal of neural and hematopoietic stem cells. *Stem Cells* **32**, 15901-15601 (2014).

11 Sheikh, B. N. *et al.* MOZ regulates B cell progenitors and, consequently, Moz haploinsufficiency dramatically retards MYC-induced lymphoma development. *Blood* **125**, 1910-1921 (2015).

12 Falk, H. *et al.* An efficient high-throughput screening method for MYST family acetyltransferases, a new class of epigenetic drug targets. *J Biomol Screen* **16**, 1196-1205 (2011).

13 Holbert, M. A. *et al.* The human monocytic leukemia zinc finger histone acetyltransferase domain contains DNA-binding activity implicated in chromatin targeting. *J Biol Chem* **282**, 36603-36613 (2007).

14 Sakaue-Sawano, A. *et al.* Visualizing spatiotemporal dynamics of multicellular cell-cycle progression *Cell* **132**, 487–498 (2008).

15 Gonzalez, S. *et al.* Oncogenic activity of Cdc6 through repression of the INK4/ARF locus. *Nature* **440**, 702-706 (2006).

16 Kueh, A. J., Dixon, M. P., Voss, A. K. & Thomas, T. HBO1 is required for H3K14 acetylation and normal transcriptional activity during embryonic development. *Mol Cell Biol* **31**, 845-860 (2011).

17 Voss, A. K., Collin, C., Dixon, M. P. & Thomas, T. Moz and retinoic acid coordinately regulate H3K9 acetylation, Hox gene expression, and segment identity. *Dev Cell* **17**, 674-686 (2009).

18 Voss, A. K. *et al.* MOZ regulates the Tbx1 locus and Moz mutation partially phenocopies DiGeorge syndrome *Dev Cell* **23**, 1-12 (2012).

19 Chew, T. W. *et al.* Crosstalk of Ras and Rho: activation of RhoA abates Kras-induced liver tumorigenesis in transgenic zebrafish models. *Oncogene* **33**, 2717-2727 (2013).

20 Adams, J. M. *et al.* The c-myc oncogene driven by immunoglobulin enhancers induces lymphoid malignancy in transgenic mice. *Nature* **318**, 533-538 (1985).

Figure legends

Figure 1: Creation of an inhibitor of the MYST family of lysine acetyltransferases.

a) Schematic summary of medicinal chemistry optimization of screening hit CTx-1024143, resulting in WM-8014 and inactive compound WM-2474. IC_{50}, determined by biochemical assays and equilibrium dissociation constants (K_D) determined by SPR are shown for KAT6A.

b) Histone acetyltransferase inhibition assay (competition of compound with AcCoA) of the initial screening hit CTx-1024143, the active compound WM-8014 and the inactive control circle area reflects IC_{50} as indicated, assayed at the AcCoA K_m for each KAT tested.

c) Dendrogram showing the relationship between major KAT families based on sequence differences in the acetyltransferase domain.

d-g) Crystal structures of WM-8014 and AcCoA bound to the MYST lysine acetyltransferase domain ($MYST^{Cryst}$; see Extended Data Fig. 1). The PDB accession codes: 6BA2 and 6BA4.

d) Space filling model showing WM-8014 in the AcCoA binding pocket of $MYST^{Cryst}$.

e) Ribbon diagram of $MYST^{Cryst}$ (blue) showing WM-8014 (yellow with element coloring) bound to the AcCoA binding site.

f) Ribbon diagram of $MYST^{Cryst}$ showing key amino acids interacting with WM-8014 (yellow with element coloring). Hydrogen bonds are shown as dashed lines.

g) Ribbon diagram showing AcCoA (yellow with element coloring) bound to $MYST^{Cryst}$.

Means of 2 experiments is shown for the IC_{50} in (**a,b**). SPR experiments were repeated four times (**a**).

Figure 2: Treatment of MEFs with WM-8014 leads to cellular senescence.

a) Effects of WM-8014 compared with inactive compound WM-2474 or vehicle DMSO on MEFs grown in 3% O_2 (left panel) and effects of dose and duration of treatment and concentration (right panel).

b) Effects of acute genetic deletion of *Kat6a* on the growth of MEFs. Loss of KAT6A function was induced by nuclear translocation of cre-recombinase using tamoxifen on MEFs isolated from $Kat6a^{lox/lox};Rosa^{CreERT2}$ and control $Rosa^{CreERT2}$ embryos.

c) Epifluorescence/phase contrast images and numerical assessment of Fucci MEFs after 6 days of treatment with 10 μM WM-8014, 10 μM WM-2474 or DMSO vehicle followed by flow cytometric analysis. DN, double negative.

d) mRNA levels of KAT6A target gene *Cdc6* mRNA and *Cdkn2a* (coding for cell cycle regulators $p16^{INK4A}$ and $p19^{ARF}$) in MEFs treated for 4 days and 10 days with 10 μM WM-8014 or 10 μM WM-2474 control assessed by RNA-sequencing.

e) Flow cytometric assessment [mean ± SEM of median fluorescent intensity (MFI)] of senescence-associated ß-galactosidase activity in MEFs after 4 and 10 days of treatment with 10 µM WM-8014, 10 µM WM-2474 or DMSO vehicle.

f) Growth of MEFs lacking $p16^{INK4A}$ and $p19^{ARF}$ and of MEFs lacking p53 vs. wild type treated with WM-8014, vehicle DMSO or WM-2474.

N = 3 independent MEF isolates per treatment group and genotype. Data are presented as mean ± SEM. Data were analyzed by one-way followed by Bonferroni post hoc test (**a-c,e**) or two-way ANOVA (**f**) with treatment with or without treatment duration as the independent factors. RNA-sequencing data (**d**) were analyzed as described in the methods section.

Figure 3: Treatment of cells with WM-8014 leads to a reduction in acetylation of specific histone lysine residues and gene expression changes that resemble genetic loss of KAT6A.

a) Western blot detecting H3K14ac or H3K9ac in MEFs treated with 10 µM WM-8014, 10 µm WM-2474 or DMSO for 5 days. N = 6 (H3K14ac) and N = 9 (H3K9ac) independent cultures per treatment group.

b) Western blot of MEFs treated with increasing doses of WM-8014 and controls as indicated. N = 3 independent experiments. Histone acetylation levels were regressed on the $\log_{10}$ of the WM-8014 concentration.

c) Barcode plot comparing genes differentially up- or downregulated in *Kat6a*$^{-/-}$ vs. *Kat6a*$^{+/+}$ MEFs, i.e. after genetic deletion of KAT6A, with genes differentially expressed in MEFs treated with WM-8014 vs. WM-2474, combined results of day 4 and day 10 treatment (ROAST p = 0.0001; N = 6 MEF isolates from 6 individual E12.5 embryos, namely from 3 *Kat6a*$^{-/-}$ and 3 *Kat6a*$^{+/+}$, as well as 3 MEF isolates from 3 wild-type embryos treated with either WM-8014 or WM-2474).

d) *Ezh2, Melk* and *E2f2* mRNA levels by RNA-sequencing in MEFs treated for 4 days and 10 days with 10 µM WM-8014 or 10 µM control WM-2474 (N = 3 MEF isolates from 3 wild-type embryos treated with either WM-8014 or WM-2474).

e) Anti-H3K9ac chromatin immunoprecipitation followed by qPCR detection of transcription start sites of genes after treatment with 10 µM WM-8014 for 3 days. The results of one of four experiments are shown; total N = 16 cultures per treatment group in 4 experiments.

Data are presented as mean ± SEM and were analyzed by one-way ANOVA followed by Bonferroni post hoc test (**a**) or two-way ANOVA (**e**) with treatment with or without gene locus as the independent factors, or by regression analysis (**b**). The RNA-sequencing analysis (**c**,**d**) is described in the methods section.

Figure 4: Treatment with WM-1119 arrests lymphoma growth.

a) Medicinal chemistry optimization of WM-8014 resulted in compound WM-1119. SPR binding data collected for WM-1119 compared to WM-8014 interaction with immobilized KAT6A, KAT7 and KAT5 shown below.

b) Growth inhibition assays of *Eμ-Myc* lymphoma cell line EMRK1184 treated with WM-1119 and WM-8014 at doses indicated.

c) Bioluminescence images of EMRK1184 lymphoma cells expressing luciferase before (day 3) and after 11 days of treatment with WM-1119 (50 mg/kg 4x/day) or PEG400 vehicle control. Red boxes show regions used for quantitation (imaging of days 7, 10, 12 in Extended Data Fig. 10).

d) Quantitation of the signals measured in all experiments: 2 cohorts mice treated 3x/day, combined N = 6; 2 cohorts of mice treated 4x/day, combined N = 9. One mouse did not respond to WM-1119 treatment, shown in grey.

e) Dissected spleens taken after imaging on Day 14 (mice shown in **c**).

f) Spleen weights of mice treated with WM-1119 or vehicle. Ns as stated in (**d**).

g) Flow cytometric analysis of spleen cells from vehicle and WM-1119 treated mice (4x/day). The tumor cells were $CD19^{+}IgM^{neg}$, and normal splenic B cells were $CD19^{+}IgM^{+}$. Quantitation of flow cytometric analysis in bone marrow (BM), spleen and peripheral white blood cells (PWBC).

N = 4 independent experiments for WM-1119 and 2 for WM-8014 in (**b**) and number of mice as indicated in (**d**,**f**,**g**) in 3 independent experiments. Data are presented as mean ± SEM and were analyzed by non-linear regression dose-response curve fit (least squares fit, inhibitor vs. response, variable slope; (**b**), one-way ANOVA followed by Bonferroni post hoc test with treatment as the independent factor (**d,g**), or two-tailed T-tests (**f**).

Data Availability Statement

The RNA sequencing data of MEFs treated with WM-8014, WM-2474 and DMSO, of MEFs from *Kat6a*$^{-/-}$ and wild type embryos and of lymphoma cell line EMRK1184 with vehicle and WM-1119 have been submitted to the GEO database under accession number GSE108244. The crystal structure data for the MYST domain in complex with WM-8014, acetyl-CoA and WM-1119 have been submitted under accession numbers PDB accession codes 6BA2, 6BA4 and 6CT2, respectively. Source data for all graphs are provided in Supplementary File "Baell Thomas source data of all graphs April 2018.xlsx".

Extended Data

Extended Data Figure 1: Binding characteristics of the MYST domain - WM-8014 protein ligand interaction and comparison of MYST family histone acetyltransferase domains

a) SPR binding data collected for WM-8014 interaction with immobilized KAT6A and KAT7. Injected concentrations of WM-8014 were 100 nM, 33 nM, 11 nM, 3.7 nM and 1.2 nM for KAT6A and 333 nM, 111 nM, 37 nM and 12 nM for KAT7. Binding responses (data; black sensorgrams) are overlaid, fitted curves of a 1:1 kinetic interaction model that included mass transport component (colored lines), as well as derived kinetic rate constants (k_a, k_d) and equilibrium dissociation (K_D) constant. One of at least 2 experiments is shown.

b) WM-8014 bound to $MYST^{Cryst}$ with the WM-8014 OMIT electron density map contoured to 3σ shown in green.

c) AcCoA bound to $MYST^{Cryst}$ with the AcCoA OMIT map contoured to 3σ shown in green.

d) Ribbon diagram showing WM-8014 and AcCoA superimposed.

e) Schematic diagram of protein-ligand interactions (LIGPLOT)[21] showing interactions between the compound WM-8014 and amino acids within the AcCoA binding pocket of the MYST domain derived from the crystal structure shown in Fig. 1. Amino acid differences between MYST family members are indicated. The crystal structure of $MYST^{Cryst}$ in complex with WM-8014 was solved by molecular replacement to 1.85 Å resolution in the $P2_12_12_1$ space group. Data collection and refinement statistics of the WM-8014 and AcCoA - co-crystal structures are listed in Supplementary Table 4. A single complex was found in the asymmetric unit and consists of residues 507-705 and 710-778 of $MYST^{Cryst}$, one WM-8014 molecule, one zinc ion, five glycerol molecules, one sodium ion, one chloride ion, and 144 water molecules. The overall structure is near identical to the $MYST^{Cryst}$:AcCoA complex. The crystal structure of the MYST domain ($MYST^{Cryst}$) in complex with AcCoA was solved by molecular replacement to 1.95 Å resolution (Supplementary Table 4). A single complex was found in the asymmetric unit and consists of residues 507-705 and 710-778 of $MYST^{Cryst}$, one AcCoA molecule, one zinc ion, three sodium ions, and 154 water molecules. The electron density map revealed obvious isomerism of the AcCoA 3-phosphate group of the ribose ring; the two isomers were each placed in to the model at 50% occupancy. The pantothenate arm of the AcCoA cofactor also adopts an identical position to published MYST HAT domain structures, though as observed previously there are differing positions for the 3'-phosphate ADP moiety likely reflecting the lack of protein interaction to this region of the molecule[13]. Autoacetylation of K604 was observed, as expected.[22] The AcCoA binding site is highly conserved between MYST domain proteins. However, there are several key

differences, which might explain the large differences in activity of WM-8014 between different family members, in particular between KAT6A and KAT8. For instance: Met648 in KAT6A is a Leu in KAT8 and Ser697 in KAT6A is a Trp in KAT8. These differences produce substantial changes in polarity adjacent to amino acids directly involved in binding. Note the proximity of Leu686 to the biphenyl ring, it is likely that the pyridazine nitrogen groups of WM-2474 disrupt this interaction rendering this compound inactive.

f) Comparison of protein sequence between the MYST family of lysine acetyltransferases within the conserved MYST domain. $MYST^{cryst}$ is a MYST domain modified to improve solubility and used in crystallization studies. Numbering is equivalent to positions in KAT6A sequence, NP_006757.2; the amino acids that interact with WM-8014 (depicted in the LIGPLOT) are shown in red.

Extended Data Figure 2: WM-8014 MEF growth inhibition time course and requirement for INK4A-ARF and p53 for WM-8014-induced cell cycle arrest.

a) MEF proliferation after treatment with three high concentrations of WM-8014. MEFs were treated either continuously for 15 days, or treatment was discontinued after 1, 2, 4 or 8 days to determine if cell could re-enter the cell cycle.

b) Phase contrast images of MEFs after 15 days of treatment with 10 μM WM-8014, 10 μM WM-2474 or DMSO vehicle, note cells with senescence morphology i.e. large nuclei indicating endoreplication without cell division and extensive cytoplasm (WM-8014 panel).

c) Cell cycle analysis of *Cdkn2a* (*Ink4a-Arf*) null and littermate control cells after treatment for 8 days with WM-8014, vehicle and inactive compound WM-2474. MEFs were exposed to BrdU for 1 h before flow cytometric analysis of BrdU incorporation during DNA synthesis (S phase) and DNA content of 2N (G0-G1) vs. 4N (G2-M) using 7-aminoactinomycin D (7-AAD).

d) Senescence-associated ß-galactosidase activity in *Cdkn2a* $^{-/-}$ and control MEFs after treatment for 15 days with 10 μM WM-8014, 10 μM WM-2474 or DMSO vehicle.

e) Cell cycle analysis of *Trp53* null MEFs and littermate control cells after treatment with WM-8014, vehicle and inactive compound WM-2474, as in (**c**).

N = 3 MEF isolates per genotype (**a**-**e**). Data are presented as mean ± SEM and by two-way ANOVA within duration of treatment with concentration and days of culture as the independent factors (**a**), by one-way ANOVA followed by Bonferroni post-hoc test (**c**-**e**).

Extended Data Figure 3: The effect of WM-8014 on cell proliferation is mediated through the cell cycle regulators $p16^{INK4A}$ and $p19^{ARF}$.

a) RT-qPCR analysis of expression levels of cell cycle regulators *Ink4a*, *Arf,* (alternative splice products of the *Cdkn2a* locus), *Ink4b* (*Cdkn2b*), and *Cdkn1a* (*p21*) mRNA in MEFs treated for 4 days and 10 days with 10 μM WM-8014 or 10 μM control WM-2474.

b) Dose-response of WM-8014 induction of *Ink4a* mRNA expression in MEFs.

c) RT-qPCR analysis of KAT6A target gene expression changes detected by RNA-seq. MEFs were treated for 4 days and 10 days with 10 μM WM-8014, 10 μM control WM-2474 or DMSO.

d) Dose-response of WM-8014-dependent reduction in *E2f2* and *Cdc6* mRNA levels in MEFs.

e) Levels of mRNA coding for MYST family proteins after treatment of MEFs for 4 days or 10 days with either WM-8014 or vehicle or inactive compound WM-2474.

N = 3 MEF isolates treated with WM-8014, WM-2474 or vehicle (**a-e**). Data are presented as mean ± SEM and analyzed by one-way ANOVA followed by Bonferroni post-hoc test (**a-d**,**e**) and by regression analysis (**d**). mRNA levels normalized to housekeeping genes (HK) were regressed on the log[concentration] of WM-8014 (**d**).

Extended Data Figure 4: WM-8014 causes cell cycle exit/senescence in MEFs, but not DNA damage or cell death

a) Flow cytometry gating strategy for the cell cycle analysis using incorporation of the nucleotide analogue BrdU to mark cells in S phase and 7-AAD to determine 2N (G0-G1) and 4N (G2-M) DNA content.

b) Flow cytometry gating strategy for the cell cycle analysis of transgenic FUCCI cells that express Azami green in mid S phase, G2 and M, Kusabira orange in mid-late G1, are double positive yellow in early S phase and double negative in early G1.

c) Assessment of DNA damage using flow cytometry to detect γH2A.X. Upper panels, MEFs exposure to UV light (positive control). Experimental samples (lower panels), quantification displayed in bar graph.

d) Flow cytometry gating strategy for cell death analysis. and representative experimental samples. Negative and positive controls (untreated and UV irradiated cells, respectively) shown in left panels.. Annexin V marks phosphatidylserine externalization on cells undergoing apoptosis, propidium iodine (PI) uptake marks cells undergoing other forms of cell death, annexin V/PI double positive, cells in late-stage apoptosis.

N = 3 cultures (**c**, **d**). Data are presented as mean ± SEM and were analyzed by one-way ANOVA with treatment as the independent factor.

Extended Data Figure 5: WM-8014 treatment induces a gene signature of cellular senescence.

a) Transcriptome analysis of MEFs treated with WM-8014 or control compound WM-2474. Multidimensional scaling plot showing a 2-dimensional clustering of MEF sample expression profiles. MEFs were isolated from 3 different C57B/6 embryos (biological replicates), numbered 5, 6 and 7 and were treated for either 4 days (96 h, red) or 10 days (240 h, green). Distances on the plot corresponding to leading $\log_2$-fold change between profiles.

b) Scatterplot showing consistency of the contrast WM-8014 vs. WM-2474 differences at the two time points. The plot shows gene-wise t-statistics for differential expression between the compounds at day 4 (x-axis) and day 10 (y-axis). Differentially expressed (DE) genes (FDR < 0.05) are highlighted. The majority of genes were equally affected by treatment after 4 or 10 days of treatment (green dots). Genes DE only at day 10 are highlighted blue, those DE only at day 4 are highlighted red.

c) Mean-difference plot of treatment $\log_2$ fold changes vs. average $\log_2$ expression. Treatment effects at 4 days and 10 days have been averaged. Differentially expressed genes are highlighted (FDR < 0.05).

d) Number of DE genes for MEFs treated with WM-8014 vs. the control compound WM-2474 (FDR < 0.05).

e) Mean-difference plot of treatment $\log_2$ fold changes vs. average $\log_2$ expression comparing between the control compound WM-2474 to vehicle (DMSO). The few DE genes (FDR < 0.05) are marked in red. No significant differences in gene expression were seen between WM-2474 and DMSO after 4 days of treatment and only 4 genes were differentially expressed after 10 days (FDR <0.05).

f) Mean-difference plot of $\log_2$ fold changes vs. average $\log_2$ expression comparing *Kat6a*$^{-/-}$ MEFs with *Kat6a*$^{+/+}$ control MEFs. Differentially expressed genes are highlighted (FDR < 0.05).

g) Genes typical of cycling cells[23] and E2F3 targets genes[24] are significantly downregulated in MEFs treated with WM-8014 compared to control compound (combined results of day 4 and day 10 treatment; ROAST gene set tests, p = 0.0001). The x-axes of the barcode plots show moderated t-statistics for the WM-8014 vs control comparison. Genes are ranked left to right from most up to most down regulated by WM-8014. Vertical bars indicate genes in the MSigDb signature sets. The worms show relative enrichment.

h) Genes that are down-regulated during p53-induced cellular senescence[25] were significantly downregulated as assessed by RNA-sequencing of MEFs treated with WM-8014 compared to control compound using the combined gene list of day 4 and day 10 treatment groups

(ROAST p = 0.0001). Genes upregulated and downregulated during cellular senescence[26] are strongly correlated with genes upregulated and downregulated, respectively between MEFs treated with 10 μM WM-8014 vs. 10 μM WM-2474 (ROAST p = 0.0039).

i) Schematic representation of cell cycle regulation, the top most enriched pathway (FDR = 1.58E-16), with 85% of the genes in this pathway downregulated after 10 days of treatment with WM-8014. DAVID[27] was used to test for functional enrichment in genes downregulated with an FDR < 0.05 by treatment with WM-8014 compared with WM-2474. Schematic drawing based on mmu04110: Cell cycle.[28] Downregulated genes are indicated in blue and genes with unchanged expression are indicated in green; in addition INK4A, ARF, INK4B and p21, which are upregulated, have been highlighted in red.

Data were collected from N = 3 MEFs isolates from 3 different embryos per treatment group, WM-8014 or WM-2474 treatment, for 96 h or 240 h (**a** to **i**).

Extended Data Figure 6: WM-8014 potentiates oncogene-induced senescence.

a) Growth curves of MEFs expressing empty vector control (pBABE) or oncogenic[29] $HRAS^{G12V}$ treated with increasing concentrations of WM-8014 as indicated or DMSO vehicle. All experiments were performed in 3% O_2.

b) WM-8014 treatment effects in a zebrafish model of hepatocellular carcinoma.[19] Doxycycline-inducible, liver-specific expression of a *GFP-kras*^{G12V} transgene leads to the accumulation of a constitutively-active, GFP-tagged form of KRAS in hepatocytes. TO-*kras*^{G12V} transgenic embryos were treated with doxycycline at 2 dpf and 5 dpf to initiate $KRAS^{G12V}$-driven hepatocyte proliferation. The size of the liver was measured by two-photon microscopy. Representative 3D reconstructions of whole livers from image stacks after treatment of transgenic zebrafish *Tg(TO-kras*^{G12V}*)* expressing $KRAS^{GV12}$ and GFP (green) in the liver or transgenic zebrafish *Tg*(*lfabp10:RFP*; *elaA:EGFP*) expressing just RFP (red).

c) Quantitation of liver volume.

d) Incorporation of the nucleotide analogue EdU after treatment of transgenic zebrafish expressing $KRAS^{G12V}$ or control fish with WM-8014 or control compound WM-2474.

e) RT-qPCR determination of *Cdkn2a* (*Ink4a*) and *Cdkn1a* (*p21*) mRNA levels in transgenic zebrafish *Tg(TO-kras*^{G12V}*)* treated as described in (**b**).

N = 6 independent cultures (**a**), 20 zebrafish (**b**,**c**), 10-12 zebrafish (**d**) and 4-5 zebrafish (**e**). Data are presented as mean ± SEM and were analyzed by two-way ANOVA (A) or one-way ANOVA (**d**,**e**) followed by Bonferroni post hoc test with treatment with or without treatment duration as the independent factors or by linear regression analysis regressing liver volume on WM-8014 concentration (**c**).

Extended Data Figure 7: Medicinal chemistry optimization of WM-8014 designed to reduce plasma protein binding resulted in the compound WM-1119.

a) SPR binding data collected for WM-1119 compared to WM-8014 interaction with immobilized KAT6A, KAT7 and KAT5.

b) Crystal structure of WM-1119 bound to the MYST lysine acetyltransferase domain ($MYST^{Cryst}$). Ribbon diagram of $MYST^{Cryst}$ (blue) showing WM-1119 (yellow with element coloring) bound to the AcCoA binding site. Data collection and refinement statistics of the WM-1119 - co-crystal structures are listed in Supplementary Table 5. The PDB accession code: 6CT2.

c) Space filling model showing WM-1119 in the AcCoA binding pocket of $MYST^{Cryst}$.

d) WM-1119 bound to $MYST^{Cryst}$ with the OMIT electron density map contoured to 3σ shown in green.

e) Ribbon diagram of $MYST^{Cryst}$ showing key amino acids interacting with WM-1119 in stick fashion with element coloring. Hydrogen bonds are shown as dashed lines.

(**f**) Schematic diagram of protein-ligand interactions (LIGPLOT)[21] showing interactions between the compound WM-1119 and amino acids within the AcCoA binding pocket of the MYST domain derived from the crystal structure.

Extended Data Figure 8: WM-1119 causes retention of cells in G_1 phase of the cell cycle.

a) WM-1119 causes cell cycle arrest in MEFs grown in 3% O_2. Epifluorescence/phase contrast images of Fucci MEFs after 8 days of treatment with 10 μM WM-1119 compared to 10 μM control WM-2474 treated cells.

b) WM-1119 was tested at concentrations from 1 to 10 μM compared to DMSO or 10 μM inactive compound WM-2474. Cell number under each condition was assessed at passage.

c) Flow cytometric analysis of Azami green (mAG1; mid S, G_2, M), Kusabira orange (mKO2; mid-late G_1), double positive yellow (early S) and double negative (DN, early G_1). Dot plots are shown for DMSO and 10 μM WM-2474 control treatment groups and after treatment with 1 μM and 2.5 μM active compound WM1119.

d) Quantitation is shown for all treatment groups in the bar graph. A higher proportion of WM-1119 treated cells is in mid-late G1.

N = 3 independent MEF isolates. Data are presented as mean ± SEM and were analyzed by by two-way ANOVA (**b**) or one-way ANOVA followed by Bonferroni post hoc test (**d**) with treatment with or without time as the independent factors.

Extended Data Figure 9: Characterization of WM-1119 and lymphoma cell line EMRK1184

a) Pharmacokinetic parameters for WM-1119 in mice following intraperitoneal injection. Note that the plasma concentration falls below 1 µM after 4 h. Data of N = 2 animals are shown.

b) Characterization of the *Eμ-Myc* lymphoma cell line EMRK1184. Western blot detecting p53 and $p19^{ARF}$. The negative control cell line EMRK1263 lacks the ARF ($p19^{ARF}$) band. Upregulation of p53 protein levels in positive control cell line EMRK1172 indicates non-functional p53 (commonly mutations in the DNA binding domain). EMRK1184 cells were sensitive to nutlin-3a-induced cell death, indicating intact p53. In contrast, EMRK1172 cells are insensitive to nutlin-3a. p53 exon sequencing of EMRK1184 using the MiSeq system (Illumina) confirmed wild-type p53 exon sequences.

c) Multidimensional scaling plot showing a 2-dimensional clustering of EMRK1184 lymphoma cell culture expression profiles. EMRK1184 lymphoma cells were treated for either 3 days or 6 days, in triplicate, with WM-1119 or vehicle before RNA-sequencing. Distances on the plot corresponding to leading $\log_2$-fold change between gene expression profiles.

d) Mean-difference plot of treatment $\log_2$ fold changes vs. average $\log_2$ expression for gene expression changes in the EMRK1184 lymphoma cell line after treatment for 3 and 6 days with WM-1119 or vehicle (DMSO). Differentially expressed genes are highlighted (FDR < 0.05).

e) mRNA levels assessed by RNA-sequencing of EMRK1184 treated with WM-1119 or vehicle. *Cdkn2a* mRNA, coding for $P16^{INK4A}$/$P19^{ARF}$, *Cdkn2b* and *Cdkn1a* mRNA levels are shown.

f) Western blot and densitometry detecting $P16^{INK4A}$ and $P19^{ARF}$ protein in EMRK1184 treated with WM-1119 or vehicle for 3 days. Each lane represents one independent culture, a total of 6 lanes = 6 cultures are shown.

Data are presented as mean ± CI (**a**) and ± SEM (**b**,**e**,**f**). Data in **b** were derived from 3 (EMRK1172) and 2 (EMRK1184) independent cell culture experiments, reflected by the individual data points. Data in **c**-**e** were derived from 3 independent cultures per treatment group and analyzed as described under RNA-sequencing. Data in **f** were analyzed by one-way ANOVA followed by Bonferroni post hoc test.

Extended Data Figure 10: WM-1119 is effective in inhibiting tumor progression.

a) Tumor development monitored by luciferase activity and bioluminescence imaging. The complete series of lateral images of mice treated 4x/day with either vehicle or WM-1119 between Day 7 and Day 14 after injection with tumor cells. Baseline tumor burden is shown at higher sensitivity setting for Day 3 (before treatment) in Fig. 4. Here images of days 7, 10, 12 and 14 after tumor cell transplant are shown on the same, less sensitive scale. Mice are imaged in the same order. Red boxes indicate the area used for quantitation.

b) Mouse body weights are not affected by treatment 3x/day or 4x/day.

c) Concentration of WM-1119 in peripheral blood and spleen 6 h after final injection (4x/day; N = 6 animals per treatment group).

d) Flow cytometry analysis of total spleen cells from vehicle or WM-1119 treated groups (4x/day; analysis of spleens assayed in **a**) to identify tumor cells independently of luciferase expression. The lymphoma cell line EMRK1184 has a cell surface phenotype of $CD19^{+}IgM^{neg}IgD^{neg}$. Flow cytometry was used to quantitate the $CD19^{+}IgD^{neg}$ population, which can be distinguished from normal splenic B cell populations, which are $CD19^{+}IgD^{+}$.

e) Intracellular flow cytometric analysis of H3K9ac in tumor cells. Histogram showing H3K9ac levels in the remaining tumor cells ($CD19^{+}IgM^{neg}$) in spleens of the WM-1119 treated mice (red profile) compared to the vehicle treated mice (blue profile). Shift in the red (WM-1119 treated) compared to the blue (vehicle) profile indicates a reduction in signal. Mean ± SEM of the median fluorescent intensity (MFI) is shown in the bar graph.

f) Peripheral blood analysis of vehicle or WM-1119 treated mice. The 3x/day treatment cohort is compared to the 4x/day cohort.

Images representative of N = 9 animals per treatment group in the 4x/day treatment regime (**a**). N = 3 animals per treatment group (b-f). Data are presented as mean ± SEM and were analyzed by one-way ANOVA with treatment as the independent factor followed by Bonferroni post hoc test (**b**), one-way ANOVA followed by Bonferroni post hoc test with treatment as the independent factor (**e**) or two (**d,f**) or one-sided T-test (**e**).

693
694 **References**

695 21 Wallace, A. C., Laskowski, R. A. & Thornton, J. M. LIGPLOT: a program to
696 generate schematic diagrams of protein-ligand interactions. *Protein Eng* **8**, 127-134
697 (1995).

698 22 Yuan, H. *et al.* MYST protein acetyltransferase activity requires active site lysine
699 autoacetylation. *EMBO J* **31**, 58-70 (2012).

700 23 Chang, H. Y. *et al.* Gene expression signature of fibroblast serum response predicts
701 human cancer progression: similarities between tumors and wounds. *PLoS Biol* **2**, E7
702 (2004).

703 24 Kong, L. J., Chang, J. T., Bild, A. H. & Nevins, J. R. Compensation and specificity of
704 function within the E2F family. *Oncogene* **26**, 321-327 (2007).

705 25 Tang, X., Milyavsky, M., Goldfinger, N. & Rotter, V. Amyloid-beta precursor-like
706 protein APLP1 is a novel p53 transcriptional target gene that augments neuroblastoma
707 cell death upon genotoxic stress. *Oncogene* **26**, 7302-7312 (2007).

708 26 Lujambio, A. *et al.* Non-cell-autonomous tumor suppression by p53. *Cell* **153**, 449-
709 460 (2013).

710 27 Huang, D. W., Sherman, B. T. & Lempicki, R. A. Systematic and integrative analysis
711 of large gene lists using DAVID bioinformatics resources. *Nat Protocol* **4**, 44-57
712 (2009).

713 28 Kanehisa, M., Sato, Y., Kawashima, M., Furumichi, M. & Tanabe, M. KEGG as a
714 reference resource for gene and protein annotation. *Nuc Acids Res* **44**, D457-462
715 (2016).

716 29 Serrano, M., Lin, A. W., McCurrach, M. E., Beach, D. & Lowe, S. W. Oncogenic Ras
717 provokes premature cell senescence associated with accumulation of p53 and
718 p16INK4a *Cell* **88**, 593–602 (1997).

719

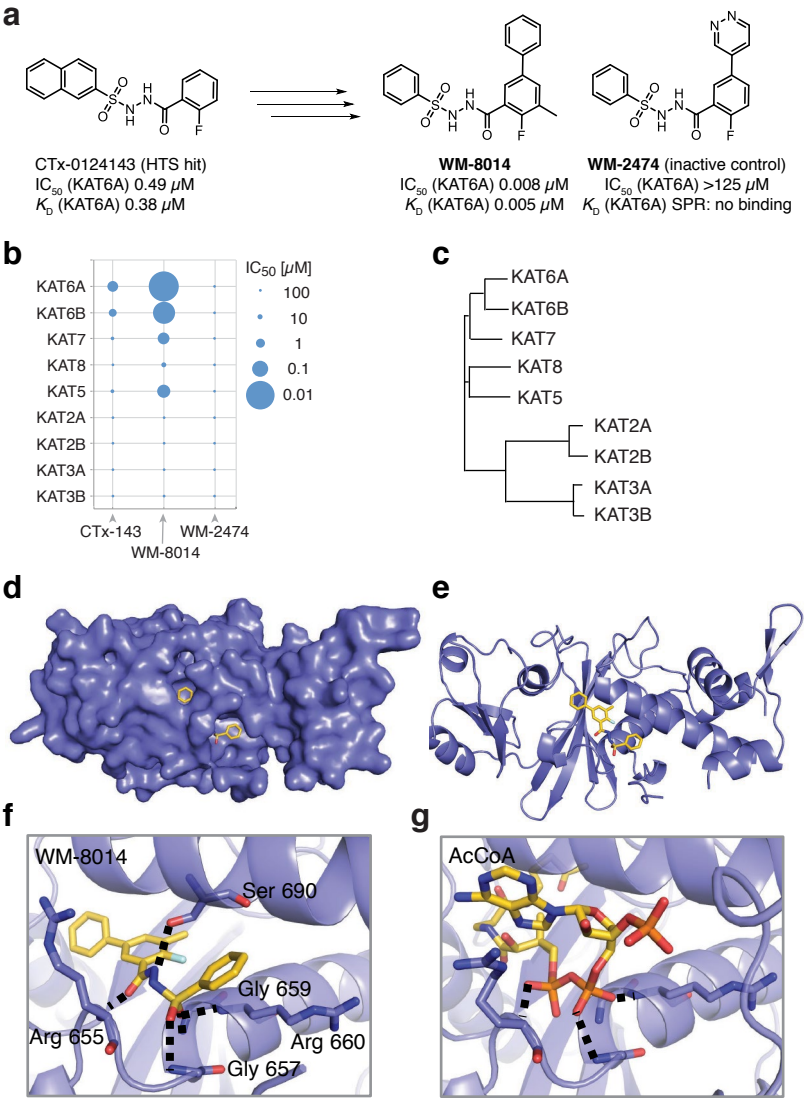
a
CTx-0124143 (HTS hit)
IC50 (KAT6A) 0.49 μM
KD (KAT6A) 0.38 μM
WM-8014
IC50 (KAT6A) 0.008 μM
KD (KAT6A) 0.005 μM
WM-2474 (inactive control)
IC50 (KAT6A) >125 μM
KD (KAT6A) SPR: no binding
b
IC50 [μM]
100
10
1
0.1
0.01
KAT6A
KAT6B
KAT7
KAT8
KAT5
KAT2A
KAT2B
KAT3A
KAT3B
CTx-143
WM-2474
WM-8014
c
KAT6A
KAT6B
KAT7
KAT8
KAT5
KAT2A
KAT2B
KAT3A
KAT3B
d
e
f
WM-8014
Ser 690
Gly 659
Arg 655
Arg 660
Gly 657
g
AcCoA

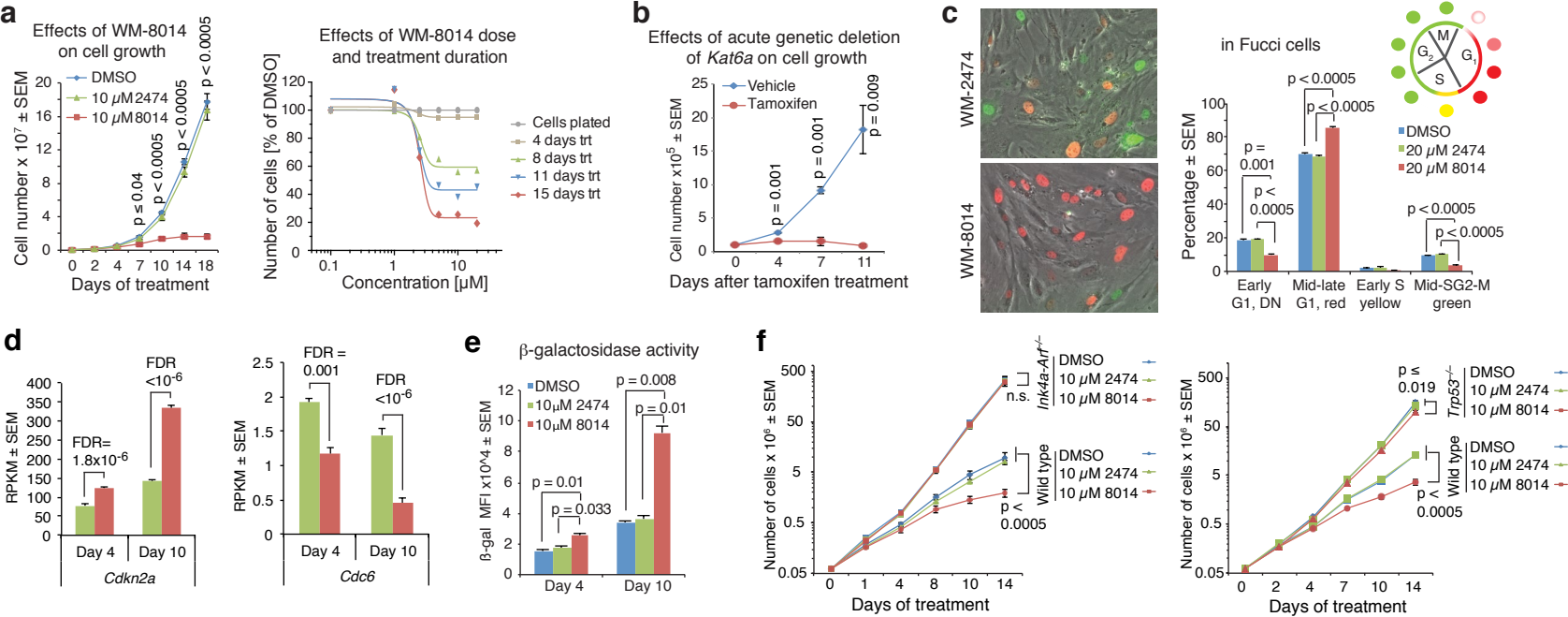
a
Effects of WM-8014 on cell growth
Cell number x 10^7 ± SEM
DMSO
10 μM 2474
10 μM 8014
p ≤ 0.04
p < 0.0005
p < 0.0005
p < 0.0005
Days of treatment
Effects of WM-8014 dose and treatment duration
Number of cells [% of DMSO]
Concentration [μM]
Cells plated
4 days trt
8 days trt
11 days trt
15 days trt
b
Effects of acute genetic deletion of Kat6a on cell growth
Cell number x10^5 ± SEM
Vehicle
Tamoxifen
p = 0.001
p = 0.001
p = 0.009
Days after tamoxifen treatment
c
WM-2474
WM-8014
in Fucci cells
Percentage ± SEM
p = 0.001
p < 0.0005
p < 0.0005
p < 0.0005
p < 0.0005
DMSO
20 μM 2474
20 μM 8014
Early G1, DN
Mid-late G1, red
Early S yellow
Mid-SG2-M green
M
G2
G1
S
d
RPKM ± SEM
FDR= 1.8x10^-6
FDR <10^-6
Day 4
Day 10
Cdkn2a
FDR = 0.001
FDR <10^-6
Day 4
Day 10
Cdc6
e
β-galactosidase activity
β-gal MFI x10^4 ± SEM
DMSO
10μM 2474
10μM 8014
p = 0.01
p = 0.033
p = 0.008
p = 0.01
Day 4
Day 10
f
Number of cells x 10^6 ± SEM
Ink4a-Arf-/-
n.s.
DMSO
10 μM 2474
10 μM 8014
Wild type
p < 0.0005
DMSO
10 μM 2474
10 μM 8014
Days of treatment
Trp53-/-
p ≤ 0.019
DMSO
10 μM 2474
10 μM 8014
Wild type
p < 0.0005
DMSO
10 μM 2474
10 μM 8014
Days of treatment

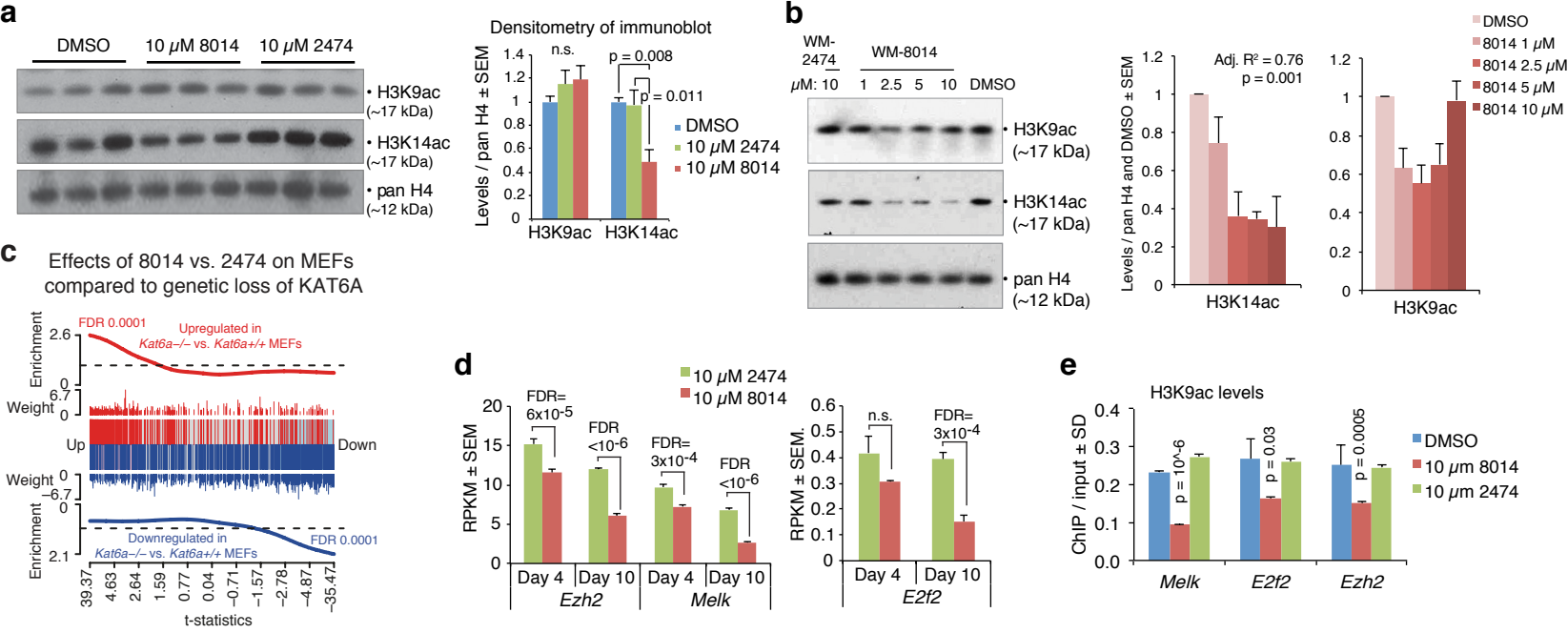
a
DMSO
10 μM 8014
10 μM 2474
• H3K9ac (~17 kDa)
• H3K14ac (~17 kDa)
• pan H4 (~12 kDa)
Densitometry of immunoblot
Levels / pan H4 ± SEM
n.s.
p = 0.008
p = 0.011
DMSO
10 μM 2474
10 μM 8014
H3K9ac
H3K14ac
b
WM-2474
WM-8014
μM: 10
1
2.5
5
10
DMSO
• H3K9ac (~17 kDa)
• H3K14ac (~17 kDa)
• pan H4 (~12 kDa)
Adj. R² = 0.76
p = 0.001
Levels / pan H4 and DMSO ± SEM
H3K14ac
H3K9ac
DMSO
8014 1 μM
8014 2.5 μM
8014 5 μM
8014 10 μM
c
Effects of 8014 vs. 2474 on MEFs compared to genetic loss of KAT6A
FDR 0.0001
Upregulated in Kat6a–/– vs. Kat6a+/+ MEFs
Enrichment
Weight
Up
Down
Downregulated in Kat6a–/– vs. Kat6a+/+ MEFs
FDR 0.0001
t-statistics
d
10 μM 2474
10 μM 8014
RPKM ± SEM
FDR= 6x10-5
FDR <10-6
FDR= 3x10-4
FDR <10-6
Day 4
Day 10
Ezh2
Melk
RPKM ± SEM.
n.s.
FDR= 3x10-4
E2f2
e
H3K9ac levels
ChIP / input ± SD
p = 10^-6
p = 0.03
p = 0.0005
DMSO
10 μm 8014
10 μm 2474
Melk
E2f2
Ezh2

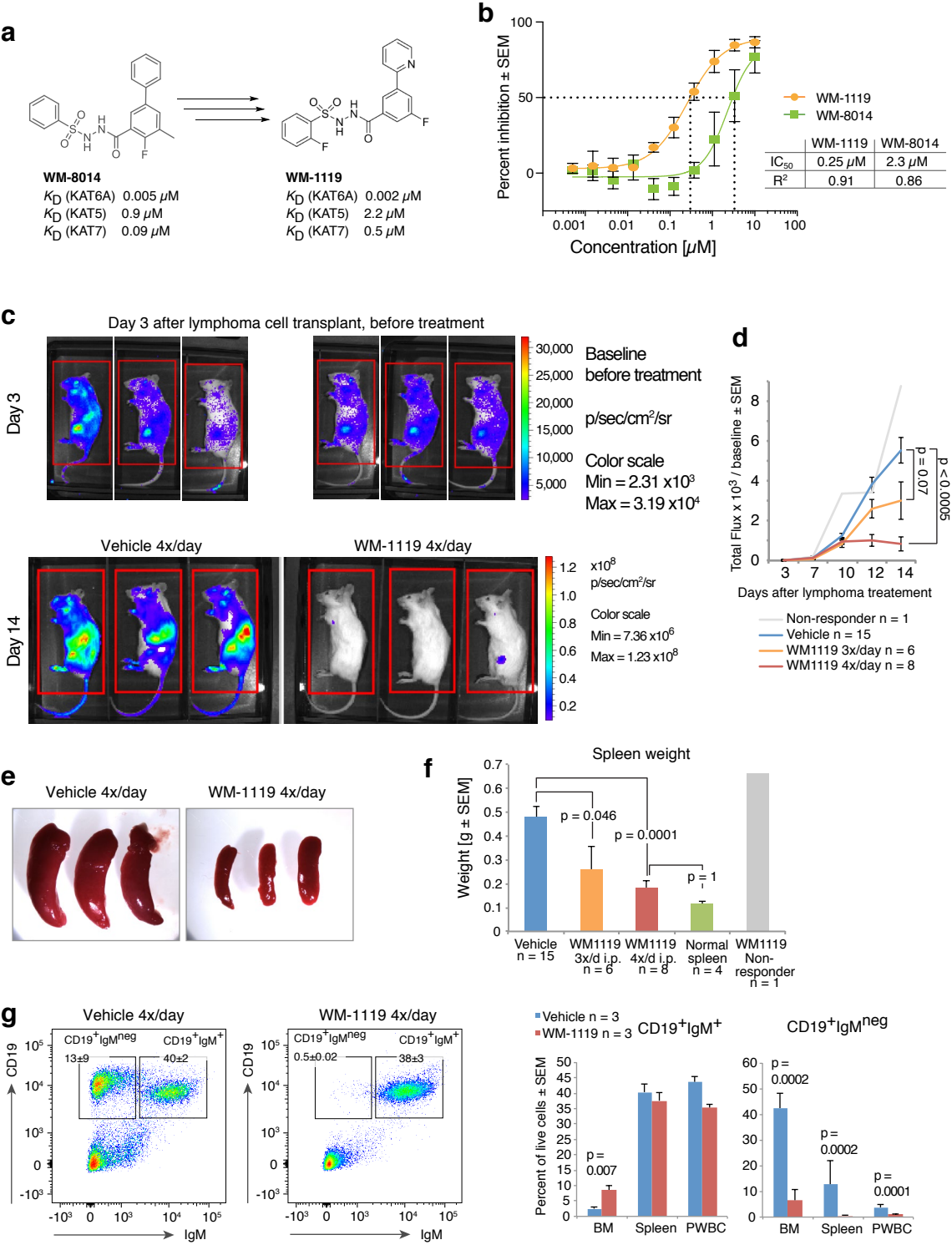
a
WM-8014
K_D (KAT6A) 0.005 μM
K_D (KAT5) 0.9 μM
K_D (KAT7) 0.09 μM
WM-1119
K_D (KAT6A) 0.002 μM
K_D (KAT5) 2.2 μM
K_D (KAT7) 0.5 μM
b
Percent inhibition ± SEM
Concentration [μM]
WM-1119
WM-8014
IC50 0.25 μM 2.3 μM
R2 0.91 0.86
c
Day 3 after lymphoma cell transplant, before treatment
Day 3
Day 14
Baseline before treatment
p/sec/cm2/sr
Color scale
Min = 2.31 x10^3
Max = 3.19 x10^4
Vehicle 4x/day
WM-1119 4x/day
x10^8 p/sec/cm2/sr
Color scale
Min = 7.36 x10^6
Max = 1.23 x10^8
d
Total Flux x 10^3 / baseline ± SEM
Days after lymphoma treatement
p = 0.07
p < 0.0005
Non-responder n = 1
Vehicle n = 15
WM1119 3x/day n = 6
WM1119 4x/day n = 8
e
Vehicle 4x/day
WM-1119 4x/day
f
Spleen weight
Weight [g ± SEM]
p = 0.046
p = 0.0001
p = 1
Vehicle n = 15
WM1119 3x/d i.p. n = 6
WM1119 4x/d i.p. n = 8
Normal spleen n = 4
WM1119 Non-responder n = 1
g
Vehicle 4x/day
WM-1119 4x/day
CD19+IgMneg
CD19+IgM+
13±9
40±2
0.5±0.02
38±3
CD19
IgM
Vehicle n = 3
WM-1119 n = 3
CD19+IgM+
CD19+IgMneg
Percent of live cells ± SEM
p = 0.007
p = 0.0002
p = 0.0002
p = 0.0001
BM
Spleen
PWBC